MATERIALS CHEMISTRY FRONTIERS

RESEARCH ARTICLE

View Article Online
View Journal

Cite this: DOI: 10.1039/d5qm00920k

Design and synthesis of a fused porphyrin dimer for enhanced visible-to-near-infrared-driven photocatalytic hydrogen evolution

Govardhana Babu Bodedla,†*[ab] Venkatesh Piradi,†[c] Muhammad Imran,[d] Jianzhang Zhao,[d] Xunjin Zhu*[ab] and Wai-Yeung Wong*[ab]

A new acceptor–linker–donor–linker–acceptor (A–π–D–π–A) structured porphyrin dimer, **F-C19ZnP**, was designed and synthesized as a visible-to-near-infrared (Vis-NIR) light-harvesting photosensitizer for photocatalytic hydrogen evolution (PHE). **F-C19ZnP** features a bimetallic Zn(II)-coordinated fused porphyrin dimer as the donor, a phenylene–ethynylene π-linker, and a 3-ethylrhodanine acceptor. Its photophysical, electrochemical, thermal, and morphological properties, as well as photocurrent response, water contact angle, and PHE performance, were systematically investigated and compared with those of **C19ZnP**, a structurally similar monometallic porphyrin. Density functional theory calculations provided further insight into the optoelectronic and charge separation characteristics of both porphyrins. **F-C19ZnP** exhibited markedly broader light absorption (400–1100 nm) and stronger Vis-NIR light-harvesting ability than **C19ZnP**. **F-C19ZnP** also exhibits a higher surface area and a larger pore size than **C19ZnP**, providing more accessible channels for electron transport. It also showed a longer photoexcited electron lifetime (4.9 ns *vs.* 2.1 ns), enabling more efficient electron transfer to water and resulting in enhanced PHE performance. **F-C19ZnP** demonstrated a higher photocurrent response, signifying improved charge separation and transport. Its lower water contact angle, attributed to its well-dispersed 300 nm nanosphere morphology, enabled better interfacial interaction with water. Under optimized PHE conditions, **F-C19ZnP** achieved a PHE rate (ηH_2) of 7.93 mmol g^{-1} h^{-1}, which is eight times higher than that of **C19ZnP** (1.01 mmol g^{-1} h^{-1}), and outperformed **C19ZnP** at all tested irradiation wavelengths (420, 630, and 810 nm). Furthermore, **F-C19ZnP** displayed excellent photostability and reusability. As the first Vis-NIR fused porphyrin dimer for efficient PHE, **F-C19ZnP** paves a promising path for the development of advanced porphyrin-based photosensitizers.

Received 24th December 2025,
Accepted 19th February 2026

DOI: 10.1039/d5qm00920k

rsc.li/frontiers-materials

Introduction

Photocatalytic hydrogen evolution (PHE) from water splitting has become a green and sustainable technology alternative to fossil fuels due to its ability to convert solar energy into chemical energy.[1–3] A photocatalytic system for water splitting typically consists of a photosensitizer, a sacrificial electron donor (SED), a cocatalyst, and water as a proton (H^+) source. Together, these components generate hydrogen (H_2) in the presence of light.[4,5] In recent years, a variety of photocatalytic systems using inorganic semiconductors,[6–11] inorganic complexes,[12,13] graphitic carbon nitride and its hybrids,[14–17] graphene-derived composites,[18,19] organic dyes,[20–22] conjugated polymers, such as conjugated porous polymers,[23–25] covalent organic frameworks,[26–28] covalent triazine frameworks,[29–31] and linear conjugated polymers,[32–35] metal–organic frameworks,[36–38] perovskite materials[39,40] and tetrapyrrole-based derivatives[5,41] as photosensitizers for PHE have been developed. Among them, tetrapyrrole-based photosensitizers such as porphyrins,[42] phthalocyanines,[43,44] and corroles,[45] on the other hand, have recently received significant attention from the scientific community due to their synthetically tunable properties, which allow them to absorb UV-to-visible (UV-Vis) light while retaining suitable energy levels to drive various photocatalytic processes. Particularly, porphyrin derivatives are excellent UV-Vis absorption materials and, like

[a] Department of Applied Biology & Chemical Technology and Research Institute for Smart Energy, The Hong Kong Polytechnic University, Hong Kong, P. R. China. E-mail: govardhana.bodedla@polyu.edu.hk, wai-yeung.wong@polyu.edu.hk
[b] The Hong Kong Polytechnic University Shenzhen Research Institute, Shenzhen 518057, P. R. China
[c] Department of Chemistry, The University of Texas at Austin, 105 E. 24th Street A5300, Austin, Texas 78712-1224, USA
[d] School of Chemical Engineering and State Key Laboratory of Fine Chemicals Dalian University of Technology, Dalian 116024, P. R. China
† These authors contributed equally.

chlorophylls, can act as natural light harvesters in photosynthesis.[5,46] In recent years, we and several other groups have diligently worked to develop effective porphyrin-based photosensitizers for PHE due to their easily adjustable optical and electrical properties through peripheral functionalization and variation of core metals, resulting in improved PHE performance.[5,47–53]

However, most of the reported porphyrins with tetra-*meso*-substituted structures have demonstrated poor visible-to-near-infrared (Vis-NIR) absorption. Since the IR region constitutes 51% of the total solar spectrum, developing Vis-NIR light-harvesting porphyrins could potentially capture up to 98% of the solar spectrum, making them highly useful for practical PHE applications. Inspired by the design of push–pull configuration-based porphyrins in photovoltaics,[54–56] we have recently reported porphyrins with an acceptor–linker–donor–linker–acceptor (A–π–D–π–A) structural configuration for enhanced PHE.[57] These A–π–D–π–A-based porphyrins exhibited light-harvesting ability in the Vis-NIR region due to intramolecular charge transfer (ICT) from the porphyrin donor moiety to the rhodanine acceptor moiety. The presence of ICT in A–π–D–π–A porphyrins not only decreases the band gap by extending the light absorption range in the solar spectrum but also promotes the photoinduced charge separation and migration of charge carriers in the porphyrins. As a consequence, A–π–D–π–A porphyrins exhibited much higher PHE performance than typical tetra-*meso*-substituted zinc(II)-coordinated tetraphenylporphyrin (ZnTPP), which possesses inferior separation and migration of photoinduced charge carriers and absorption in the UV-Vis region only due to the lack of D–A interactions.

Therefore, we were motivated to develop a porphyrin dimer, **F-C19ZnP**, with an A–π–D–π–A configuration featuring a bimetallic Zn(II)-coordinated fused porphyrin dimer donor entity and enhanced Vis-NIR absorption for PHE (Fig. 1). Compared to the porphyrin monomer **C19ZnP**, which contains a monometallic Zn(II)-coordinated porphyrin donor moiety, the porphyrin dimer **F-C19ZnP** exhibits enhanced light-harvesting ability in the Vis-NIR region, a longer photoexcited state lifetime, and suitable redox potentials due to its rigid, extended π-conjugated core and bimetallic system. Furthermore, **F-C19ZnP** demonstrates efficient separation and migration of photoinduced charge carriers, as well as a lower water contact angle than **C19ZnP**.[58–62] **F-C19ZnP** also possesses a higher surface area and a larger pore size than **C19ZnP**, offering more accessible pathways for electron transport. The porphyrin dimer **F-C19ZnP** achieves a PHE rate (ηH_2) of 7.93 mmol g^{-1} h^{-1}, which is much higher than that of the control porphyrin monomer **C19ZnP**, which has an ηH_2 of 1.01 mmol g^{-1} h^{-1}. Notably, although fused copper(II)-coordinated porphyrin-based conjugated polymer thin films have been developed for both electrocatalytic H_2 evolution (EHE) and PHE,[63] and directly fused copper(II)-coordinated porphyrin dimers have been reported for EHE,[64] these materials do not possess an A–π–D–π–A configuration. To the best of our knowledge, no research on the use of A–π–D–π–A-based porphyrin dimers with a bimetallic Zn(II)-coordinated fused porphyrin dimer donor entity as photosensitizers in PHE has been reported so far.

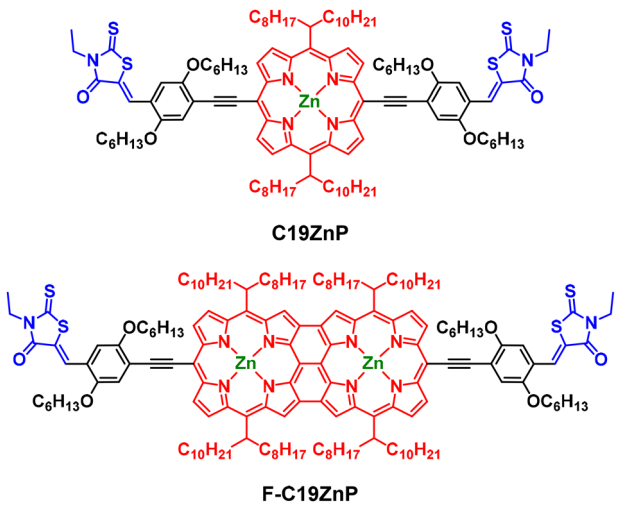

Fig. 1 Structures of A–π–D–π–A-based porphyrins used in this study.

Results and discussion

Experimental section

The synthesis of **F-C19ZnP** is shown in Scheme 1. **F-C19ZnP** was unambiguously characterized by nuclear magnetic resonance (NMR) and matrix-assisted laser desorption ionization time-of-flight mass spectrometry (MALDI-TOF). Notably, in the ^{1}H NMR spectrum of porphyrin monomer **3**, the *meso* proton resonance is observed at 10.06 ppm, while the corresponding β-pyrrolic protons appear in the 9.88–9.33 ppm region (Fig. S14). Upon formation of the triply fused porphyrin **4**, the *meso* proton signal disappears, consistent with C–C bond formation at the *meso* positions, and the β–β and β′–β′ proton resonances exhibit slight shifts to the 9.89–9.29 ppm range (Fig. S16). **F-C19ZnP** is highly soluble in chloroform, dichloromethane, and tetrahydrofuran (THF) solvents. Porphyrin scaffold **1** was synthesized and characterized according to the previous report. **C19ZnP** was also synthesized for comparison.[65]

Photophysical and electrochemical properties

Fig. 2(a) shows the absorption spectra of **C19ZnP** and **F-C19ZnP** recorded in THF solution, with the corresponding data presented in Table 1. Both porphyrins exhibit two main types of absorption peaks. The absorption peaks appearing in the shorter wavelength regions (*ca.* 400–550 nm) correspond to the Soret-band of the porphyrin moiety, while the peaks located in the longer wavelength regions (*ca.* 600–850 nm) correspond to the Q-band of the porphyrin moiety. Moreover, the Soret- and Q-band peaks of **F-C19ZnP** are significantly more red-shifted than those of **C19ZnP**. This could be attributed to the strong electron-donating nature of the bimetallic fused porphyrin dimer donor moiety, which can enhance the ICT from the bimetallic fused porphyrin donor moiety to the rhodanine

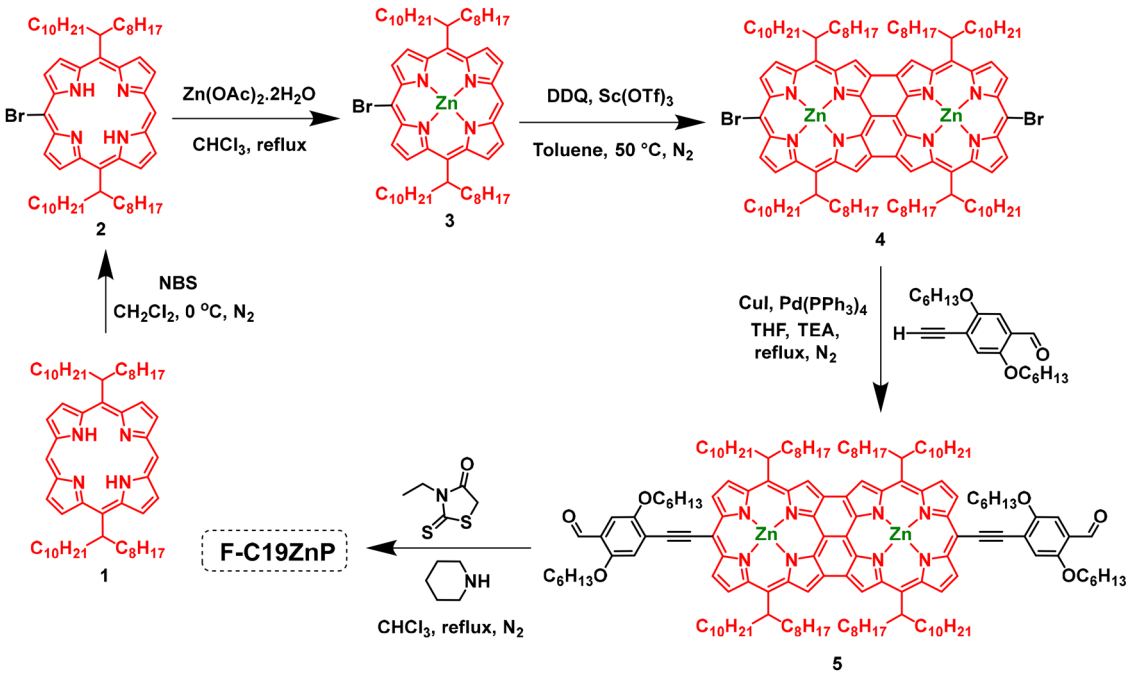

Scheme 1 Synthetic route of the fused porphyrin dimer **F-C19ZnP**.

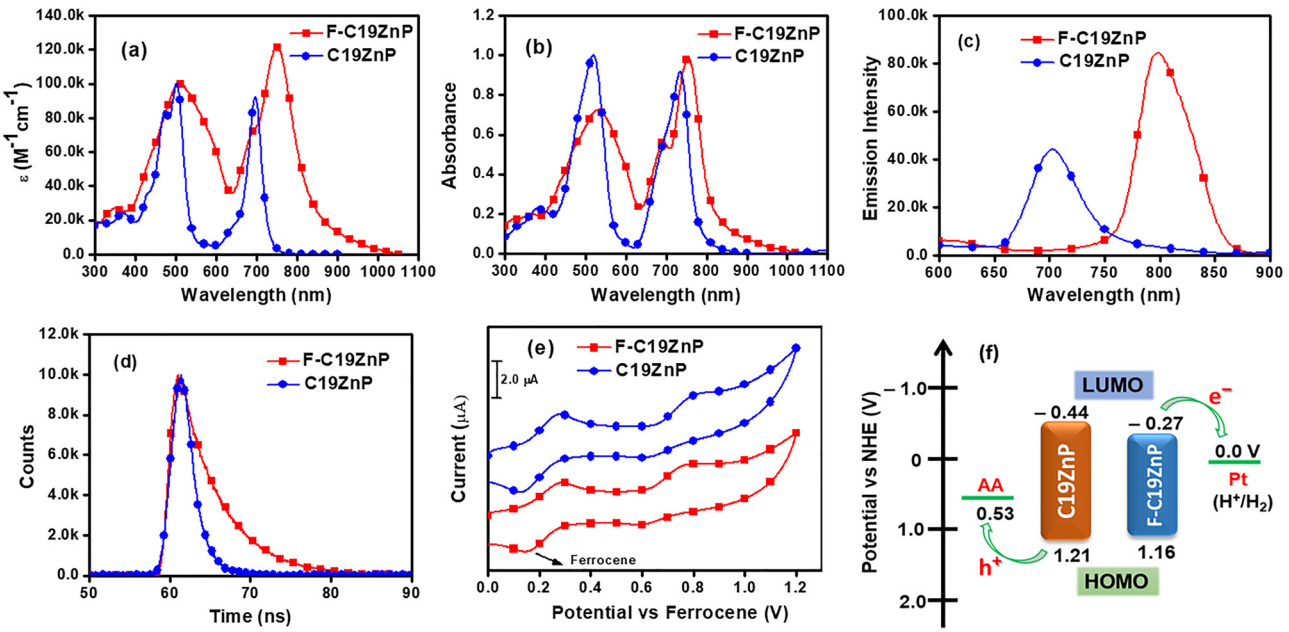

Fig. 2 Absorption spectra of **C19ZnP** and **F-C19ZnP** recorded in (a) THF solution (10 μM) and (b) the solid state (100 μM) at room temperature, (c) emission spectra of porphyrins recorded in THF solution (10 μM), (d) photoluminescence lifetime decay spectra of porphyrins recorded in THF solution (10 μM) (λ_{ex} = 380 nm), (e) cyclic voltammograms of **C19ZnP** and **F-C19ZnP** recorded in THF solution (200 μM) and (f) energy level alignment of components used in the PHE systems.

acceptor through phenylene-ethylene π-linkers in the A–π–D–π–A architecture. Notably, **F-C19ZnP** covers a broad absorption profile from 400 to 1100 nm, while **C19ZnP** exhibits an absorption profile from 400 to 800 nm with a deep valley in the range of 550–650 nm. This indicates that **F-C19ZnP** features stronger Vis-NIR light absorption than **C19ZnP**, which is far more beneficial for capturing more photons from the solar spectrum and, therefore, enhances the solar-driven applications of **F-C19ZnP**. However, when the absorption spectra of both porphyrins were recorded in the solid state (Fig. 2(b)), they displayed red-shifted Soret- and Q-bands compared to those in the THF solution, illustrating the formation of J-type aggregates

Table 1 Photophysical, electrochemical and thermal data of C19ZnP and **F-C19ZnP**

Porphyrin	λ_{abs}[a] (nm) (ε, $\times 10^4$ M^{-1} cm^{-1})	λ_{abs}[b] (nm)	λ_{em}[a] (nm)	τ_{PL}[a] (ns)	Φ_{PL} (%)[a]	k_{nr} ($\times 10^8$ s^{-1})	T_d (°C)	E_{OX} (V)	E_{HOMO}[c] (V) (*vs.* NHE)	E_{LUMO}[d] (V) (*vs.* NHE)	$E_{0\text{-}0}$[e] (eV)
F-C19ZnP	516 (9.90), 692 (7.31), 752 (12.11)	540, 695, 760	804	4.9	15	1.69	400	0.39	1.16	−0.27	1.43
C19ZnP	472 (8.41), 500 (10.0), 696 (9.23)	518, 734	702	2.1	10	4.23	345	0.44	1.21	−0.44	1.65

[a] THF solution. [b] Spin-coated thin films. [c] E_{HOMO} (*vs.* NHE) = 0.77 + E_{OX} (*vs.* ferrocene). [d] E_{LUMO} (*vs.* NHE) = E_{HOMO} − $E_{0\text{-}0}$. [e] Determined from the intersection of the tangent of the absorption peak and the *x*-axis by 1240/λ.

in the solid state. This is commonly observed for rod-shaped A–π–D–π–A porphyrins in the solid state.[57]

The emission spectra of **F-C19ZnP** and **C19ZnP**, recorded under excitation at 500 nm, which correspond to the Soret band of the porphyrin moiety, are shown in Fig. 2(c). Both porphyrins, **F-C19ZnP** and **C19ZnP**, showed emission peaks at 800 nm and 700 nm, respectively. Notably, **F-C19ZnP** exhibited an intensified emission peak with a 100 nm red-shift compared to **C19ZnP**. The red-shifted emission wavelength of **F-C19ZnP** compared to **C19ZnP** aligns well with the trends observed in the absorption peaks. The intensified emission peak of **F-C19ZnP** compared to **C19ZnP** indicates that the insertion of a fused porphyrin donor moiety in the A–π–D–π–A structure can suppress non-radiative and charge recombination channels due to the rigidity of the fused porphyrin donor moiety. The calculated photoluminescence electron lifetime (τ_{PL}) of **F-C19ZnP** is 4.9 ns, which is much longer than that of **C19ZnP** (2.1 ns) (Fig. 2(d)). The photoluminescence quantum yields (Φ_{PL}) of **F-C19ZnP** and **C19ZnP** were calculated to be 15% and 10%, respectively, which is consistent with the τ_{PL} of the porphyrins. These results precisely match the above description and help provide a long-lived photoexcited state τ_{PL} value for **F-C19ZnP**, consequently indicating its potential use as a photosensitizer over **C19ZnP** in PHE application. Moreover, based on the τ_{PL} and Φ_{PL} values, we have calculated the nonradiative decay constant (k_{nr}) for both porphyrins.[66] **F-C19ZnP** shows a k_{nr} value of 1.69 × 10^8 s^{-1}, which is much lower than that of **C19ZnP** (4.23 × 10^8 s^{-1}). This further demonstrates that **F-C19ZnP** reduces nonradiative decay channels more effectively than **C19ZnP**. On the other hand, the Φ_{PL} and τ_{PL} values of **F-C19ZnP** are much higher than those of our previously reported more efficient A–π–D–π–A porphyrin ZnP-CPDT with a cyclopentadithiophene (CPDT) π-linker (Φ_{PL} = 8.0%, τ_{PL} = 1.51 ns).[57] Thus, designing and synthesizing A–π–D–π–A porphyrins using a bimetallic fused porphyrin donor moiety is a very important strategy for achieving long-lived photoexcited states in A–π–D–π–A porphyrins.

The cyclic voltammograms of **F-C19ZnP** and **C19ZnP** recorded in THF solution are shown in Fig. 2(e), and the corresponding data are presented in Table 1. **F-C19ZnP** and **C19ZnP** exhibited oxidation potential (E_{OX}) values of 0.39 V and 0.44 V, respectively. The lower E_{OX} value of **F-C19ZnP** compared to **C19ZnP** can be attributed to the greater reducing ability of the electron-rich bimetallic fused porphyrin donor moiety compared to the monometallic porphyrin donor moiety. Based on the E_{OX} values, the calculated E_{HOMO} values of **F-C19ZnP** and **C19ZnP** porphyrins are 1.16 V and 1.21 V, respectively. On the other hand, the E_{LUMO} values of **F-C19ZnP** and **C19ZnP** were calculated using the equation: E_{LUMO} = E_{HOMO} − $E_{0\text{-}0}$.[67,68] The E_{LUMO} values of **F-C19ZnP** and **C19ZnP** were calculated to be −0.27 V and −0.44 V, respectively. The results indicate that **F-C19ZnP** and **C19ZnP** possess suitable E_{HOMO} and E_{LUMO} values for efficient charge separation and migration of holes and electrons, which is followed by PHE in the presence of a Pt cocatalyst and an ascorbic acid (AA) SED (Fig. 2(f)).

Morphological and thermal properties

The solid state morphology of **F-C19ZnP** and **C19ZnP** was studied using scanning electron microscopy (SEM) analysis. Porphyrin-coated thin films were prepared by drop-casting THF solutions of the porphyrins onto silica substrates. As shown in Fig. 3(a)–(d), both porphyrins formed nanospheres in the solid state. However, it was found that **F-C19ZnP** formed well-dispersed nanospheres with a size of approximately 300 nm, whereas **C19ZnP** exhibited stacked nanospheres with variable sizes ranging from 50 to 500 nm. This indicates that **F-C19ZnP** possesses a more controlled morphology in terms of both size and shape. Such morphology is much more beneficial for facilitating contact between water and a greater number of **F-C19ZnP** molecules. In contrast, the stacked nanosphere morphology of **C19ZnP** can limit the exposure of its molecules to water. Thus, a higher PHE performance is expected for **F-C19ZnP** than for **C19ZnP** during photocatalytic water splitting (*vide infra*). To further understand the morphology of the porphyrins, we performed powder X-ray diffraction (PXRD) analysis. As shown in Fig. 3(e), neither **F-C19ZnP** nor **C19ZnP** exhibited any sharp peaks. This indicates that both **F-C19ZnP** and **C19ZnP** possess an amorphous nature.

Furthermore, to evaluate the relative porosities of **C19ZnP** and **F-C19ZnP**, N_2 adsorption–desorption isotherms were collected at 78 K (Fig. S3, SI). **C19ZnP** exhibits very low N_2 uptake across the entire pressure range, indicating a slightly nonporous solid. In contrast, **F-C19ZnP** shows higher gas uptake, consistent with the presence of greater porosity. Brunauer–Emmett–Teller (BET) analysis gives specific surface areas of 6.47 m^2 g^{-1} for **C19ZnP** and 18.12 m^2 g^{-1} for **F-C19ZnP**, confirming the higher accessible surface area of the fused porphyrin dimer. Correspondingly, pore size distribution analysis using the Horváth–Kawazoe method revealed dominant micropores of approximately 6.13 Å for **F-C19ZnP** and 2.98 Å for **C19ZnP**. The higher BET surface area and larger pore size of **F-C19ZnP** compared to **C19ZnP** can provide more accessible channels for electron transport and, subsequently, more efficient H^+ reduction and thus enhanced PHE (*vide infra*).

The thermal decomposition temperatures (T_d) of **F-C19ZnP** and **C19ZnP** were evaluated using thermogravimetric analysis

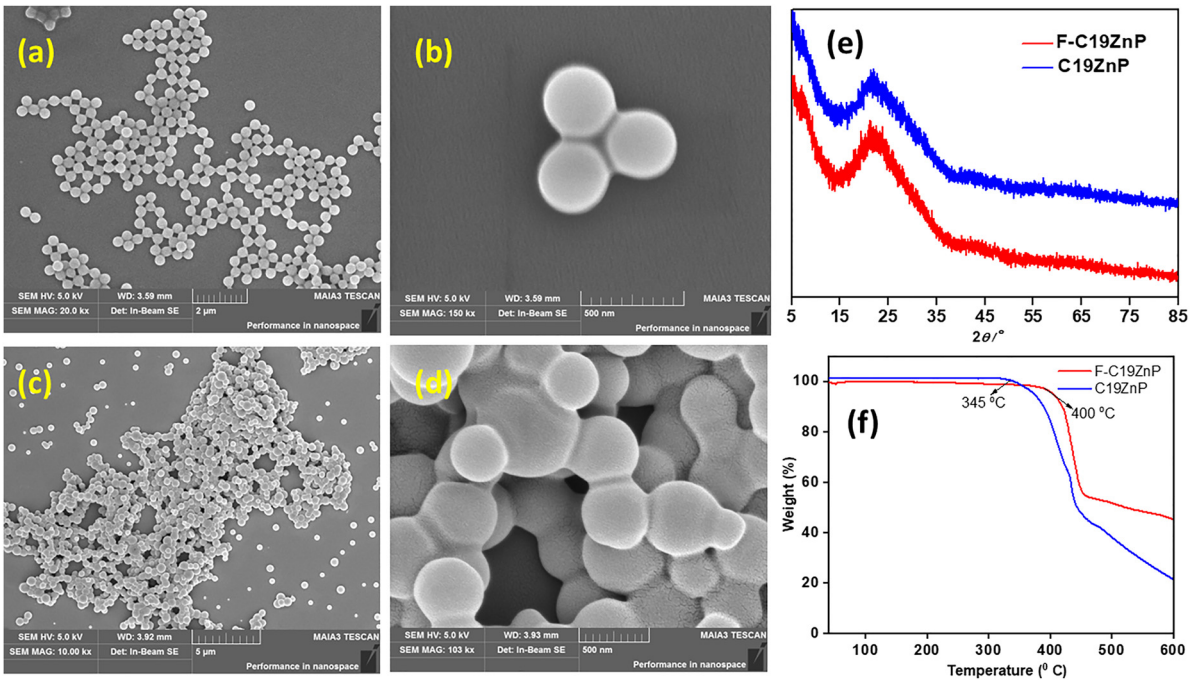

Fig. 3 Typical SEM images of (a) and (b) **F-C19ZnP** and (c) and (d) **C19ZnP** (note: all the images were taken for drop-cast thin films of porphyrins from their THF solution (100 μM)), (e) typical PXRD patterns of the porphyrins and (f) TGA curves of **F-C19ZnP** and **C19ZnP**.

(TGA) measurements. As shown in Fig. 3(f), **F-C19ZnP** and **C19ZnP** exhibited T_d values of 400 °C and 345 °C, respectively. This demonstrates that **F-C19ZnP**, with its bimetallic fused porphyrin donor moiety, possesses higher thermal stability than **C19ZnP**, which has a monometallic porphyrin donor moiety. This result clearly indicate that designing A–π–D–π–A porphyrins with a rigid fused porphyrin donor moiety is an ideal strategy for constructing thermally stable photoactive systems.

Density functional theory (DFT) calculations

To understand the electronic structure, possible ICT behavior, and photoinduced charge separation properties of **F-C19ZnP** and **C19ZnP**, we performed DFT calculations. The front and side views of both porphyrins, **F-C19ZnP** and **C19ZnP**, exhibited planar conformations with varying angles (Fig. 4(a)). The dihedral angles between the two fused porphyrin moieties in **F-C19ZnP** are 0.29° and −0.22°. The dihedral angles at the edge of the π-linker are 0.05° and 0.17° for **F-C19ZnP** and **C19ZnP**, respectively. Moreover, the bond angle between the fused porphyrin donor moiety and the linker part is lower in **F-C19ZnP** compared to that in **C19ZnP**. This can enhance the ICT between the fused porphyrin donor moiety and the acceptor part through the π-linker. Thus, the calculated wavelengths of the absorption peaks of **F-C19ZnP** are red-shifted compared to those of **C19ZnP** (Fig. S1 and Table 2). This result is consistent with the experimentally observed red-shifted absorption peaks of **F-C19ZnP** relative to **C19ZnP**.

Moreover, the frontier molecular orbitals of both porphyrins are shown in Fig. 4(b). In both compounds, the highest occupied molecular orbital (HOMO) and lowest unoccupied molecular orbital (LUMO) are mainly localized over the central porphyrin macrocycle, indicating that the core unit dominates the primary optical transitions. To better assess the potential for ICT upon photoexcitation, particularly in the context of the molecular complexity of **F-C19ZnP**, we further examined the neighboring orbitals. The HOMO−1 remains localized on the porphyrin core, while the LUMO+1 orbital shows significant localization on the peripheral substituents, especially on the π-linker and the 3-ethylrhodanine acceptor group. This spatial distinction implies that while the initial HOMO–LUMO transition is localized on the central porphyrin unit, subsequent relaxation enables ICT from the electron-rich porphyrin core towards the electron-deficient 3-ethylrhodanine group. Given the strong electron-withdrawing nature of the rhodanine unit, it influences the stabilization of the LUMO+1 orbital, which participates in ICT, especially in a polar microenvironment. Moreover, the π-conjugated linker between the porphyrin donor macrocycle and rhodanine acceptor groups facilitates electronic communication, supporting multi-orbital-mediated charge separation pathways. This highlights the role of the π-linker and the 3-ethylrhodanine acceptor in modulating the photophysical behavior.

To gain more insight into charge distribution and donor–acceptor interactions within the **F-C19ZnP** and **C19ZnP** porphyrins, electrostatic potential (ESP) maps were constructed (Fig. S2). These maps visualize the spatial distribution of electron-rich and electron-deficient regions and the direction of ICT. In both molecules, the electron-rich regions (indicated by blue surfaces) lie on the central porphyrin core, whereas the electron-deficient regions (shown by red surfaces) are situated on the phenylene–ethynylene π-linker and 3-ethylrhodanine edges on both sides of the central porphyrin core. This distribution

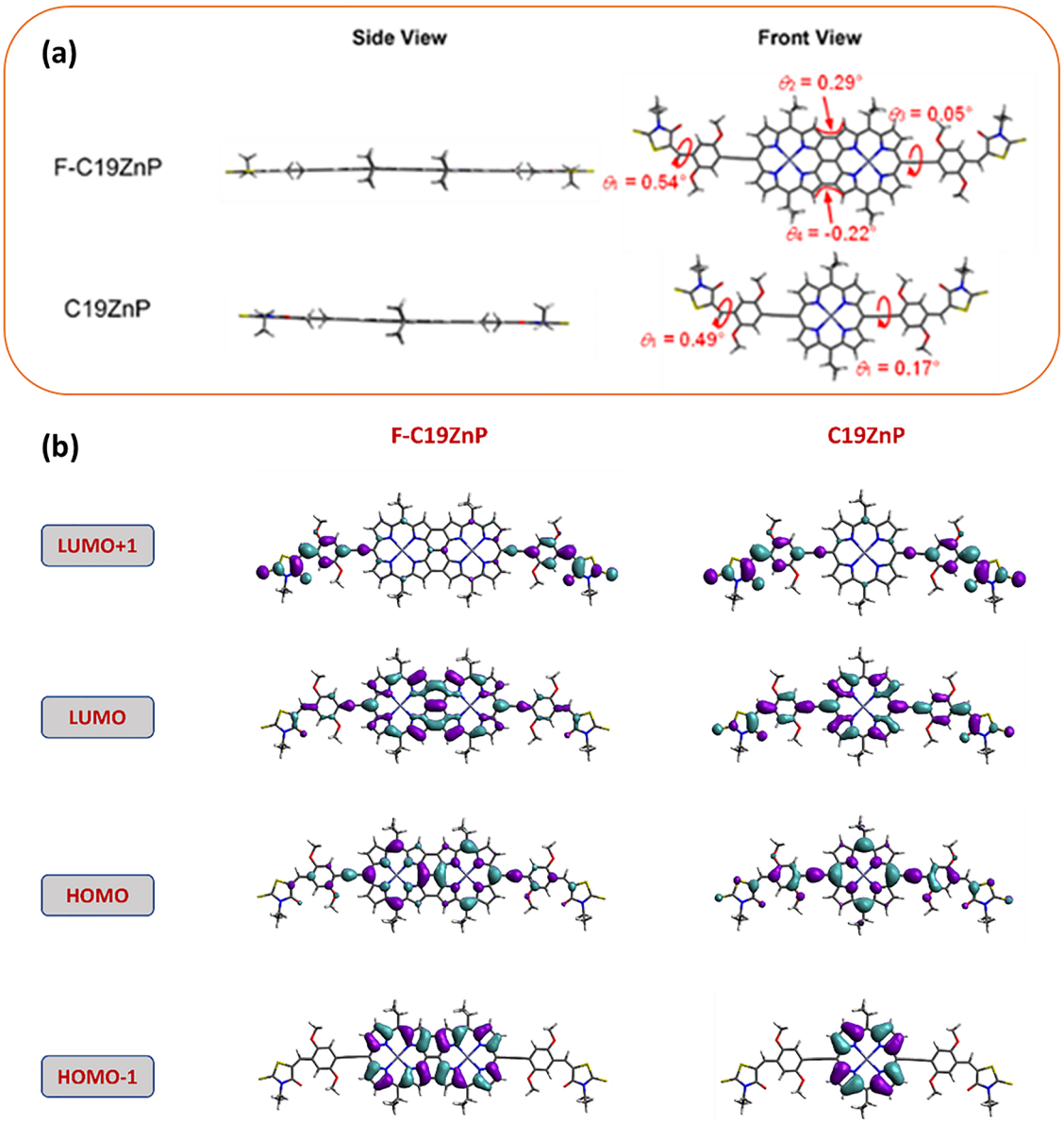

Fig. 4 (a) Ground state optimized molecular geometries of **F-C19ZnP** and **C19ZnP** (the hydrogen atoms are omitted for clarity and the long alkyl chains are simplified to methyl groups to reduce the calculation time) and (b) selected frontier molecular orbitals of **F-C19ZnP** and **C19ZnP**. Note: calculations were performed using the Gaussian 16 Rev B01 program package at the DFT-CAMB3LYP/GENECP/LANL2DZ level in the gas phase.

demonstrates electronic polarization across the conjugated framework, indicating a net electron transfer from the porphyrin donor towards the terminal acceptor moieties upon photoexcitation. Efficient electron delocalization from the porphyrin core to the outer acceptors facilitates the stabilization of the charge-separated state, which can promote the H^+ reduction reaction for cocatalyst-supported PHE efficiency. This delocalization can further suppress the charge recombination process, which is beneficial for photocatalytic performance (*vide infra*).

The calculated dipole moments of **F-C19ZnP** and **C19ZnP** are 2.94 D and 2.93 D, respectively, which are very close. This implies that both porphyrins possess nearly identical ground-state polarity despite structural modification. This suggests that the incorporation of a fused porphyrin–linker framework in **F-C19ZnP** does not significantly change the overall direction and magnitude of the ground-state charge distribution compared with **C19ZnP**. In other words, the spatial arrangement of electron-donating and electron-withdrawing units leads to a comparable dipole vector orientation and extent.

PHE studies

The PHE performance of **F-C19ZnP** and **C19ZnP** porphyrins was evaluated by employing them as photosensitizers/photocatalysts in a heterogeneous photocatalytic system. In this setup, THF is used as a water-miscible solvent to achieve a facile dispersion of the porphyrins in water. Water serves as the H^+ source, AA acts as the SED, and platinum (Pt) nanoparticles are employed as the cocatalyst. The entire system is irradiated with

Table 2 Calculated electronic transition properties of the low-lying electronic excited states of **F-C19ZnP** and **C19ZnP** at the B3LYP/GENECP/LANL2DZ level

Porphyrin	State	Electronic transition	Energy[a] (eV/nm)	f[b]	Composition[c]	CI[d]
F-C19ZnP	Singlet	$S_0 \rightarrow S_1$	1.16/1068	1.6259	H → L	0.68367
		$S_0 \rightarrow S_6$	1.91/647	1.5350	H → L+2	0.61919
		$S_0 \rightarrow S_{13}$	2.30/537	1.4471	H−2 → L+1	0.53836
	Triplet	$S_0 \rightarrow T_1$	0.90/1377	0.0000	H−1 → L	0.67844
		$S_0 \rightarrow T_2$	1.24/994	0.0000	H−2 → L	0.56899
		$S_0 \rightarrow T_3$	1.44/856	0.0000	H → L+3	0.65680
C19ZnP	Singlet	$S_0 \rightarrow S_1$	1.68/733	2.2447	H → L	0.69292
		$S_0 \rightarrow S_6$	2.48/499	0.5025	H−3 → L	0.61432
		$S_0 \rightarrow S_{11}$	2.65/466	0.5416	H−2 → L+1	0.40831
		$S_0 \rightarrow S_{14}$	2.91/425	0.7744	H−7 → L	0.45020
	Triplet	$S_0 \rightarrow T_1$	1.08/1143	0.0000	H → L	0.66896
		$S_0 \rightarrow T_2$	1.48/835	0.0000	H → L+1	0.44665
		$S_0 \rightarrow T_3$	1.52/813	0.0000	H−1 → L	0.45921

[a] Only the selected low-lying excited states are presented. [b] Oscillator strength. [c] Only the main configurations are presented. [d] The CI coefficients are in absolute values. Note: H and L indicate the HOMO and LUMO, respectively, and S and T indicate the singlet and triplet states, respectively.

full-spectrum LED white light. To prepare the PHE systems, THF solutions of the porphyrins are added to water, resulting in the dispersion of the porphyrins, which subsequently self-assemble into nanoaggregates within the THF/water (1 : 1, v/v) solvent mixture. These nanoaggregates impart a heterogeneous character to the photocatalytic system. The formation of such aggregates is crucial, as they provide active catalytic sites similar to those found in conventional heterogeneous powder photocatalysts. This aggregation greatly improves the interaction between the photocatalyst and water, thereby facilitating efficient PHE under photocatalytic conditions. From Fig. 5(a), it can be observed that **F-C19ZnP** produced an ηH_2 of 7.93 mmol g^{-1} h^{-1}, which is 8-fold higher than that of **C19ZnP** (1.01 mmol g^{-1} h^{-1}). Moreover, the ηH_2 of **F-C19ZnP** is also 4.5-fold higher than that of our previously reported more efficient A–π–D–π–A porphyrin ZnP-CPDT with a CPDT π-linker (1.80 mmol g^{-1} h^{-1}).[57] The higher ηH_2 of **F-C19ZnP** compared to **C19ZnP** can be attributed to the following factors: (i) strong light-harvesting ability in the Vis-NIR

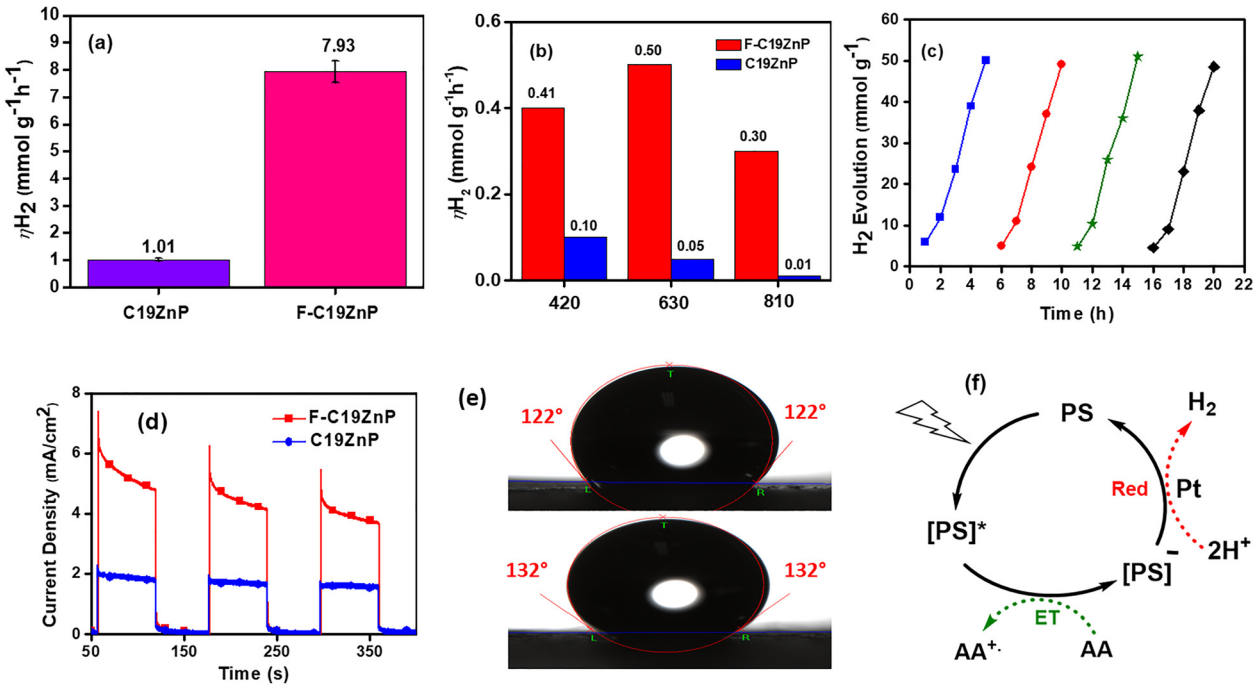

Fig. 5 (a) The ηH_2 of photocatalytic systems of **C19ZnP** and **F-C19ZnP** under irradiation for 5 h: **C19ZnP**/**F-C19ZnP** (0.1 mM) + AA (0.4 M) + THF/water (1 : 1, v/v) + Pt (3 wt%), white LED light (full spectrum, 148.5 mW cm^{-2}), (b) ηH_2 of photocatalytic systems of **C19ZnP** and **F-C19ZnP** under irradiation for 5 h: **C19ZnP**/**F-C19ZnP** (0.1 mM) + AA (0.4 M) + THF/water (1 : 1, v/v) + Pt (3 wt%), white LED light (420 nm (68 mW cm^{-2}), 630 nm (49 mW cm^{-2}) and 810 nm (46 mW cm^{-2})), (c) H_2 evolution of different cycles of the **F-C19ZnP** photocatalytic system: **F-C19ZnP** (0.1 mM) + AA (0.4 M) + THF/water (1 : 1, v/v) + Pt (3 wt%), white LED light (full spectrum); 0.4 M AA was re-added after the third cycle, (d) I–t response spectra of porphyrins; (e) water contact angle measurements of **F-C19ZnP** (top) and **C19ZnP** (bottom) in water; and (f) feasible PHE mechanism of photocatalytic systems. PS represents the photosensitizer, ET refers to electron transfer, and "Red" represents reduction.

region, (ii) long-lived photoexcited state τ_{PL} value, (iii) well-defined nanosphere morphology with uniform size (*vide supra*), (iv) high BET surface area and large pore size (*vide supra*), (v) efficient separation and migration of photoinduced charge carriers, (vi) low electron transport resistance (R_{ct2}), and (vii) lower water contact angle (*vide infra*). Besides, the photocatalytic system of **F-C19ZnP** did not produce any H_2 in the absence of the AA SED and the Pt cocatalyst. This indicates that AA is crucial for reducing **F-C19ZnP**, and the Pt cocatalyst helps enhance charge separation in the photoexcited states of **F-C19ZnP** and the reduction of H^+ to H_2. To further optimize the PHE of **F-C19ZnP**, the ηH_2 of **F-C19ZnP** photocatalytic systems was recorded at different concentrations of AA and variable amounts of Pt loading while keeping the **F-C19ZnP** concentration constant (0.1 mM) in a THF/water mixture (1 : 1, v/v). As shown in Fig. S4(a), the ηH_2 of **F-C19ZnP** photocatalytic systems increases with increasing AA concentration from 0.1 M to 0.4 M, but further increases in AA concentration decrease ηH_2. On the other hand, the ηH_2 of the photocatalytic system of **F-C19ZnP** increases with increasing Pt loading from 1 to 3 wt%, but further increases in Pt loading reduce ηH_2 (Fig. S4(b)). These results indicate that the **F-C19ZnP** photocatalytic system containing 0.4 M of AA and 3 wt% of Pt is the best-optimized condition for achieving high PHE. The PHE performance of **F-C19ZnP** was also tested in the presence of different SEDs such as triethylamine (TEA), triethanolamine (TEOA), and ethylenediaminetetraacetic acid (EDTA). Fig. S5 shows that the ηH_2 of photocatalytic systems containing TEA, TEOA, and EDTA is much lower than that of photocatalytic systems containing AA. This indicates that AA is the ideal SED for achieving enhanced PHE performance of the **F-C19ZnP** porphyrin. Using the optimized conditions mentioned above (0.4 M AA and 3 wt% Pt) for the **F-C19ZnP** photocatalytic system, the PHE performance of **F-C19ZnP** was further tested under different ratios of THF/water mixtures (Fig. S6). The results show that a 1 : 1 (v/v) THF/water mixture is the ideal solvent composition to achieve efficient PHE for **F-C19ZnP**.

To further understand the relationship between light-harvesting ability and PHE performance, we explored the wavelength-dependent ηH_2 of both **F-C19ZnP** and **C19ZnP** (Fig. 5(b)). These measurements were conducted under optimized conditions and full-spectrum white LED light irradiation for both photocatalytic systems of **F-C19ZnP** and **C19ZnP**. For **F-C19ZnP**, the ηH_2 values achieved were 0.41, 0.50, and 0.30 mmol g^{-1} h^{-1} at the wavelengths of 420 nm, 630 nm, and 810 nm, respectively, under white LED light irradiation. In contrast, **C19ZnP** produced significantly lower ηH_2 values of 0.10, 0.05, and 0.01 mmol g^{-1} h^{-1} at the same wavelengths. These results clearly establish the superior photocatalytic performance of **F-C19ZnP** across the Vis-NIR region compared to **C19ZnP**. More notably, the PHE performance of **F-C19ZnP** in the NIR region (specifically at 810 nm) is comparable to its activity in the visible region (420 nm and 630 nm). This signifies that **F-C19ZnP** maintains efficient PHE even under longer-wavelength light irradiation, a feature that is highly required for solar energy applications. In contrast, **C19ZnP** shows negligible PHE activity in the NIR region, demonstrating its limited light-harvesting range. These conclusions provide convincing evidence that the design and development of A–π–D–π–A-based porphyrins, predominantly those incorporating a bimetallic fused porphyrin donor moiety, represent a highly effective strategy for extending PHE activity into the NIR region. Such molecular engineering not only broadens the light absorption spectrum but also significantly enhances the PHE performance.

The apparent quantum yield (AQY) of **F-C19ZnP** was calculated to be 1.64%, 2.0%, and 1.2% at 420, 630, and 810 nm, respectively, while the AQY values of **C19ZnP** were 0.39%, 0.20%, and 0.04% at the same wavelengths (Fig. S7). These results are highly consistent with their observed PHE performance, further demonstrating the superior ability of **F-C19ZnP** to utilize NIR photons compared to **C19ZnP**. The photostability of **F-C19ZnP** was tested by recording the PHE of the **F-C19ZnP** photocatalytic system over 40 h of light irradiation. As shown in Fig. S8, the PHE of the **F-C19ZnP** photocatalytic system continuously increased with time, indicating excellent photostability of **F-C19ZnP** under prolonged light irradiation conditions. Additionally, the reusability of **F-C19ZnP** was tested by analyzing the PHE of the **F-C19ZnP** photocatalytic system over four consecutive photocyclic experiments under 20 h of light irradiation (Fig. 5(c)). In each cycle, the **F-C19ZnP** photocatalytic system produced similar ηH_2, indicating the good reusability of **F-C19ZnP**. Furthermore, we analyzed the morphology data of **F-C19ZnP** before and after 20 h of light irradiation in its photocatalytic system. Fig. S9 shows that the nanosphere morphology of **F-C19ZnP** did not change before and after photocatalysis, further confirming the photostability of **F-C19ZnP** under PHE conditions.[51] To further assess the stability of **F-C19ZnP** during PHE, we recorded the UV-Vis absorption spectra of the photocatalytic system before and after 40 h of irradiation, as shown in Fig. S10. The absorption profile of **F-C19ZnP** remained nearly unchanged after prolonged light irradiation, confirming its excellent photostability. This result indicates that the porphyrin structure, including the Zn(II) center, remains intact under the reaction conditions. While we did not directly measure the Zn ion concentration in solution, the preserved absorption features strongly suggest that no significant decomposition or demetallation of the catalyst occurred during the photocatalytic process.

In heterogeneous PHE, the separation and migration of photoinduced charge carriers from the surface of the photosensitizer to the cocatalyst and SED influence the efficiency of H_2 evolution in photocatalytic systems.[69] To investigate how efficiently charge carrier separation and transport can occur for **C19ZnP** and **F-C19ZnP**, we performed photocurrent–time (*i*–*t*) response and Nyquist plot studies. Porphyrins coated on indium tin oxide (ITO) substrates were used to analyze the *i*–*t* curve responses and Nyquist plots. As shown in Fig. 5(d), **F-C19ZnP** exhibited a higher photocurrent density compared to **C19ZnP**, signifying the efficient separation and migration of photoinduced charge carriers, such as hole–electron pairs, for the former porphyrin. Additionally, we recorded a Nyquist plot of porphyrins under illumination conditions to estimate the electron transport rate. From Fig. S11, it can be seen that a

smaller radius of the circle was observed for **F-C19ZnP** in comparison to **C19ZnP**. This demonstrates that **F-C19ZnP** possesses a lower R_{ct2} than **C19ZnP** and, therefore, enhanced electron migration within **F-C19ZnP** under illumination conditions. Since **F-C19ZnP** possesses efficient hole–electron pair separation and higher electron transport than **C19ZnP**, the availability of electrons for transfer from the **F-C19ZnP** surface to the Pt cocatalyst is sufficiently high. This subsequently enhances the reduction of H^+ to H_2. This result aligns with the higher PHE of the photocatalytic system of **F-C19ZnP** compared to the **C19ZnP** photocatalytic system.

Water contact angle measurements were performed to elucidate the interface between the porphyrins and water. As shown in Fig. 5(e), **F-C19ZnP** exhibited a water contact angle of 122°, which is lower than that of **C19ZnP** (132°), indicating that **F-C19ZnP** interacts more readily with water compared to **C19ZnP**. This enhanced interaction facilitates a more efficient electron transfer rate from photoexcited **F-C19ZnP** to H^+, resulting in improved PHE performance. The well-dispersed nanosphere morphology of **F-C19ZnP** in water likely promotes easier access of water molecules to the photocatalyst surface, whereas the strongly stacked nanosphere morphology of **C19ZnP** restricts interactions at the interface between **C19ZnP** and water (*vide supra*), highlighting the crucial role of porphyrin morphology in enhancing PHE activity. Furthermore, the higher BET surface area and larger pore size of **F-C19ZnP** (*vide supra*) compared to **C19ZnP** offer more accessible channels for electron transport and, consequently, more efficient H^+ reduction and enhanced PHE (*vide supra*). The increased surface area provides more active sites for water molecules to interact with the photocatalyst, while the larger pore size allows water to penetrate more easily into the interior part of the material, accelerating the accessibility of active sites within the pores. Both factors contribute to better dispersion of **F-C19ZnP** than **C19ZnP** in water and facilitate mass transfer, ultimately enhancing the overall PHE performance of **F-C19ZnP**. Improved wettability further ensures that the **F-C19ZnP** surface remains well-hydrated, which is essential for efficient charge transfer and the generation of reactive species during photocatalytic water splitting.

Besides, it should be noted that while our study demonstrates that **F-C19ZnP** forms well-dispersed nanospheres with uniform size, which likely facilitates better interaction with water and improved PHE performance, we propose that direct evidence connecting morphology to primary photophysical properties, such as longer τ_{PL} and enhanced charge separation, can be demonstrated based on the following experimental results. Absorption and emission studies (Fig. 2(a–c) and Table 1) reveal that **F-C19ZnP** exhibits significantly red-shifted and intensified Soret- and Q-band peaks, broader light absorption, and a longer τ_{PL} compared to **C19ZnP**. These features, along with a lower k_{nr} and a higher Φ_{PL}, indicate suppressed charge recombination and more efficient charge separation. Photocurrent and Nyquist analyses further confirm superior charge carrier separation and electron transport in **F-C19ZnP**. The well-dispersed nanosphere morphology, higher BET surface area, and larger pore size of **F-C19ZnP** likely enhance water accessibility and electron transfer, indirectly supporting improved photophysical behavior. Although a direct fundamental relationship between morphology and photophysical properties requires further investigation, our results strongly suggest that the controlled nanosphere morphology of **F-C19ZnP** complements its intrinsic photophysical advantages, leading to superior PHE performance.

To gain more insight into the PHE of porphyrins, we proposed a reasonable cyclic mechanism for the photocatalytic systems, as illustrated in Fig. 5(f). In the first step, upon light irradiation, porphyrins undergo photoexcitation; in the second step, the photoexcited porphyrins are reduced by gaining electrons from AA; and in the final step, the reduced porphyrins return to the ground state by donating electrons to the Pt cocatalyst for H^+ reduction. In our previous studies, we have already demonstrated that the reduction of photoexcited porphyrins by SEDs such as AA and TEA can occur during the cyclic PHE mechanism.[50,69–71] Additionally, our photocatalytic experiments show that H_2 evolution does not occur in the absence of AA, indicating its essential role as an SED. The significant enhancement in ηH_2 with AA, compared to other SEDs, further supports its involvement in the reduction process. Notably, the photophysical properties of **F-C19ZnP**, such as the longer τ_{PL} and higher Φ_{PL}, suggest efficient charge separation and suppressed recombination, which are consistent with effective electron transfer from AA to the photoexcited porphyrin. Thus, based on all these results, we assume that the reduction of photoexcited porphyrins by AA is involved in the cyclic PHE mechanism, as demonstrated in the proposed mechanism in Fig. 5(f).

Conclusions

In summary, we designed and synthesized a new A–π–D–π–A-based porphyrin dimer, **F-C19ZnP**, featuring a bimetallic Zn(II)-coordinated fused porphyrin dimer donor entity, and studied its optoelectronic, thermal, morphological, and PHE properties. These were compared with those of the **C19ZnP**, which has a monometallic Zn(II)-coordinated porphyrin donor moiety. **F-C19ZnP** showed a stronger Vis-NIR light-harvesting ability (400–1100 nm) than **C19ZnP**, which has visible light absorption ability (400–800 nm). Additionally, **F-C19ZnP** exhibited a longer photoexcited τ_{PL} than **C19ZnP** due to the rigid bimetallic fused porphyrin dimer donor moiety. Moreover, **F-C19ZnP** formed well-dispersed nanospheres with a size of 300 nm in the solid state, whereas stacked nanospheres with various sizes (50–300 nm) were observed for **C19ZnP**. Furthermore, the well-dispersed nanosphere morphology of **F-C19ZnP** in water facilitated easy access of water molecules to the surface of **F-C19ZnP**. In contrast, **C19ZnP**, with its strongly stacked nanosphere morphology, restricted the interactions at the interface between **C19ZnP** and water. This also demonstrates that the morphology of porphyrins plays a key role in understanding the interface between porphyrins and water. **F-C19ZnP** further demonstrates increased surface area and pore size relative to **C19ZnP**, which

enhance the accessibility of channels for electron transport. *I–t* and Nyquist plot studies revealed that **F-C19ZnP** displayed efficient photoinduced charge separation and a lower R_{ct2} than **C19ZnP**, resulting in higher electron transport mobility in its photocatalytic systems. DFT calculations further supported the enhanced light-harvesting capability and photoinduced charge separation of **F-C19ZnP**. Under PHE conditions, **F-C19ZnP** produced an η_{H_2} of 7.93 mmol g^{-1} h^{-1}, which is 8-fold higher than that of **C19ZnP** (1.01 mmol g^{-1} h^{-1}). Additionally, **F-C19ZnP** also exhibited comparable PHE performance in the NIR region to that in the visible region, whereas negligible PHE performance in the NIR region was observed for **C19ZnP**. This illustrates that developing bimetallic fused porphyrin dimers represents a highly effective strategy for extending PHE activity from the visible to the NIR region. The PHE system of **F-C19ZnP** is highly photostable, as evidenced by enhanced H_2 evolution from the initial time to 40 h of light irradiation. Research on the effect of different metal centres in the fused porphyrin donor moiety and various linkers on the PHE performance of fused porphyrin dimers is underway in our laboratory.

Author contributions

G. B. Bodedla and V. Piradi designed, synthesized, and characterized (by NMR and MALDI-TOF) all the materials used in this study. They also performed experiments such as UV-Vis, photoluminescence, cyclic voltammetry, SEM, *i–t* response and Nyquist plot studies, water contact angle measurements, and PHE experiments, and wrote the original manuscript. M. Imran performed the DFT calculations and analyzed the results. J. Zhao supervised the DFT studies. W.-Y. Wong and X. Zhu supervised the research project and revised the manuscript. All the authors discussed the results and evaluated the manuscript.

Conflicts of interest

There are no conflicts to declare.

Data availability

The data supporting this article have been included as part of the supplementary information (SI). Supplementary information: materials and methods, synthesis, photocatalytic systems under different conditions, DFT calculations, NMR spectra, and MALDI-TOF spectra. See DOI: **https://doi.org/10.1039/d5qm00920k**.

Acknowledgements

G. B. B. acknowledges the financial support from the Start-up Fund for RAPs under the Strategic Hiring Scheme (P0048725) of the Hong Kong Polytechnic University. W. -Y. W. acknowledges the financial support from the RGC Senior Research Fellowship Scheme (SRFS2021-5S01), the Research Centre for Carbon-Strategic Catalysis (CE01 and CE41), the Hong Kong Polytechnic University (YXA2), the Research Institute for Smart Energy (CDAQ) and Ms Clarea Au for the Endowed Professorship in Energy (847S). X. Z. acknowledges the funding from the General Research Fund (HKBU12304320), the NSFC/RGC Joint Research Scheme (N_HKBU213/22), and the Initiation Grant for Faculty Niche Research Areas (IG-FNRA) (2020/21)-RC-FNRA-IG/20-21/SCI/06 from Hong Kong Baptist University.

Notes and references

1 A. Fujishima and K. Honda, Electrochemical photolysis of water at a semiconductor electrode, *Nature*, 1972, **238**, 37–38.
2 T. Hisatomi and K. Domen, Reaction systems for solar hydrogen production via water splitting with particulate semiconductor photocatalysts, *Nat. Catal.*, 2019, **2**, 387–399.
3 W. Zhang, W. Lai and R. Cao, Energy-related small molecule activation reactions: oxygen reduction and hydrogen and oxygen evolution reactions catalyzed by porphyrin- and corrole-based systems, *Chem. Rev.*, 2017, **117**, 3717–3797.
4 K. Maeda and K. Domen, Photocatalytic water splitting: recent progress and future challenges, *J. Phys. Chem. Lett.*, 2010, **1**, 2655–2661.
5 G. B. Bodedla, X. Zhu and W.-Y. Wong, Recent progress in the development of self-assembled porphyrin derivatives for photocatalytic hydrogen evolution, *EnergyChem*, 2024, **6**, 100138.
6 Y. Goto, T. Hisatomi, Q. Wang, T. Higashi, K. Ishikiriyama, T. Maeda, Y. Sakata, S. Okunaka, H. Tokudome, M. Katayama, S. Akiyama, H. Nishiyama, Y. Inoue, T. Takewaki, T. Setoyama, T. Minegishi, T. Takata, T. Yamada and K. Domen, A particulate photocatalyst water-splitting panel for large scale solar hydrogen generation, *Joule*, 2018, **2**, 509–520.
7 J. Li, P. Jiménez-Calvo, E. Paineau and M. N. Ghazzal, Metal chalcogenides based heterojunctions and novel nanostructures for photocatalytic hydrogen evolution, *Catalysts*, 2020, **10**, 89.
8 X. Chen, S. Shen, L. Guo and S. S. Mao, Semiconductor-based photocatalytic hydrogen generation, *Chem. Rev.*, 2010, **110**, 6503–6570.
9 S. S. Mani, S. Rajendran, T. Mathew and C. S. Gopinath, A review on the recent advances in the design and structure activity relationship of TiO_2-based photocatalysts for solar hydrogen production, *Energy Adv.*, 2024, **3**, 1472–1504.
10 Z. Chen, Y. Yan, J. Luo, P. Shan, C. Lu, F. Guo and W. Shi, Piezoelectric effect synergistically boosted NIR-driven photothermal-assisted photocatalytic hydrogen evolution, *Chin. Chem. Lett.*, 2025, **36**, 111302.
11 S. Yan, L. Wang, P. Shan, X. Lin and W. Shi, Enhanced photocatalytic hydrogen generation *via* up-conversion in Y_2O_3:Yb^{3+}, Er^{3+} nanoparticles under near-infrared light irradiation, *Chem. Res. Chin. Univ.*, 2025, **41**, 859–867.
12 D. N. Tritton, F.-K. Tang, G. B. Bodedla, F.-W. Lee, C.-S. Kwan, K. C.-F. Leung, X. Zhu and W.-Y. Wong,

Development and advancement of iridium(III)-based complexes for photocatalytic hydrogen evolution, *Coord. Chem. Rev.*, 2022, **459**, 214390.

13 G. B. Bodedla, D. N. Tritton, X. Chen, J. Zhao, Z. Guo, K. C.-F. Leung, W.-Y. Wong and X. Zhu, Cocatalyst-free photocatalytic hydrogen evolution with simple heteroleptic iridium(III) complexes, *ACS Appl. Energy Mater.*, 2021, **4**, 3945–3951.

14 S. Tang, Y. Zhu, H. Li, H. Xu and S. Yuan, Two-dimensional carbon nitride-based composites for photocatalytic hydrogen evolution, *Int. J. Hydrogen Energy*, 2019, **44**, 30935–30948.

15 S. Tian, S. Chen, X. Ren, R. Cao, H. Hu and F. Bai, Two dimensional carbon nitride-based composites for photocatalytic hydrogen evolution, *Nano Res.*, 2019, **12**, 3109–3115.

16 L. Li, G. B. Bodedla, Z. Liu and X. Zhu, Naphthalimide porphyrin hybridized graphitic carbon nitride for enhanced photocatalytic hydrogen production, *Appl. Surf. Sci.*, 2020, **499**, 143755.

17 W.-L. Shi, Z. Xu, Y.-X. Shi, L.-L. Li, J.-L. Lu, X.-H. Sun, X. Du, F. Guo and C.-Y. Lu, Constructing S-scheme charge separation in cobalt phthalocyanine/oxygen-doped g-C_3N_4 heterojunction with enhanced photothermal-assisted photocatalytic H_2 evolution, *Rare Met.*, 2024, **43**, 198–211.

18 M. A. Mudassir, Z. Tazeen, S. Kousar, M. Li and X. Zhao, Metal–organic framework/graphene-based nanocatalysts for hydrogen evolution reaction: a comprehensive review, *Int. J. Hydrogen Energy*, 2025, **98**, 1299–1313.

19 E. Nikoloudakis, A. G. Coutsolelos and E. Stratakis, Mini review on catalytic hydrogen evolution from porphyrin graphene structures, *Energy Fuels*, 2024, **38**, 19222–19235.

20 S. Liu, P. Lin, M. Wu, Z.-A. Lan, H. Zhuzhang, M. Han, Y. Fan, X. Chen, X. Wang, Q. Li and Z. Li, Organic dyes with multi branched structures for highly efficient photocatalytic hydrogen evolution under visible-light irradiation, *Appl. Catal., B*, 2022, **309**, 121257.

21 Y. H. Hong, Y.-M. Lee, W. Nam and S. Fukuzumi, Photocatalytic hydrogen evolution from plastoquinol analogues as a potential functional model of photosystem I, *Inorg. Chem.*, 2020, **59**, 14838–14846.

22 M. Ming, H. Yuan, S. Yang, Z. Wei, Q. Lei, J. Lei and Z. Han, Efficient red-light-driven hydrogen evolution with an anthraquinone organic dye, *J. Am. Chem. Soc.*, 2022, **144**, 19680–19684.

23 S. Qiao, M. Di, J.-X. Jiang and B.-H. Han, Conjugated porous polymers for photocatalysis: the road from catalytic mechanism, molecular structure to advanced applications, *EnergyChem*, 2022, **4**, 100094.

24 C. Han, S. Xiang, S. Jin, C. Zhang and J.-X. Jiang, Rational design of conjugated microporous polymer photocatalysts with definite D–π–A structures for ultrahigh photocatalytic hydrogen evolution activity under natural sunlight, *ACS Catal.*, 2023, **13**, 204–212.

25 S. Luo, Z. Zeng, G. Zeng, Z. Liu, R. Xiao, P. Xu, H. Wang, D. Huang, Y. Liu, B. Shao, Q. Liang, D. Wang, Q. He, L. Qin and Y. Fu, Recent advances in conjugated microporous polymers for photocatalysis: designs, applications, and prospects, *J. Mater. Chem. A*, 2020, **8**, 6434–6470.

26 K. Prakash, B. Mishra, D. D. Díaz, C. M. Nagaraja and P. Pachfule, Strategic design of covalent organic frameworks (COFs) for photocatalytic hydrogen generation, *J. Mater. Chem. A*, 2023, **11**, 14489–14538.

27 M. Chen, G.-e Fu, W. Zhao and T. Zhang, Effective strategies in covalent organic frameworks for enhanced photocatalytic hydrogen production, *Chem. – Eur. J.*, 2025, **31**, e202500100.

28 A. Rodríguez-Camargo, K. Endo and B. V. Lotsch, Celebrating ten years of covalent organic frameworks for solar energy conversion: past, present and future, *Angew. Chem., Int. Ed.*, 2024, **63**, e202413096.

29 J. Yu, X. Sun, X. Xu, C. Zhang and X. He, Donor–acceptor type triazine-based conjugated porous polymer for visible-light driven photocatalytic hydrogen evolution, *Appl. Catal., B*, 2019, **257**, 117935.

30 A. Hayat, H. Ali, Z. Ajmal, A. Alshammari, M. M. Alghamdi, A. A. El-Zahhar, N. Almuqati, M. Sohail, A. M. Abu-Dief, S. Khan, Y. Al-Hadeethi, M. Z. Ansari and Y. Orooji, Emerging breakthroughs in covalent triazine frameworks: From fundamentals towards photocatalytic water splitting and challenges, *Prog. Mater. Sci.*, 2025, **147**, 101352.

31 M. Liu, F. Zhao, Y. Chu, J. Zhao, F. Meng and Y. Han, Construction of thiazolo[5,4-*d*]thiazole based covalent triazine framework/g-C_3N_4 heterojunction catalysts for highly efficient photocatalytic H_2 evolution, *Chem. Eng. Sci.*, 2024, **288**, 119827.

32 F. Mi, N. Zhao, L. Jin, Z. Zhang, X. Wang, X. Fang, W. Li, Z. Liu, P. Shu, X. Zhang and C. Wu, Conjugated polymers as photocatalysts for hydrogen therapy, *BMEMat.*, 2025, **3**, e12126.

33 Y. Liu, B. Li and Z. Xiang, Pathways towards Boosting Solar Driven Hydrogen Evolution of Conjugated Polymers, *Small*, 2021, **17**, 2007576.

34 J. Jayakumar and H.-H. Chou, Recent Advances in Visible Light-Driven Hydrogen Evolution from Water using Polymer Photocatalysts, *ChemCatChem*, 2020, **12**, 689–704.

35 J. Kosco, S. Gonzalez-Carrero, C. T. Howells, T. Fei, Y. Dong, R. Sougrat, G. T. Harrison, Y. Firdaus, R. Sheelamanthula, B. Purushothaman, F. Moruzzi, W. Xu, L. Zhao, A. Basu, S. De Wolf, T. D. Anthopoulos, J. R. Durrant and I. McCulloch, Generation of long-lived charges in organic semiconductor heterojunction nanoparticles for efficient photocatalytic hydrogen evolution, *Nat. Energy*, 2022, **7**, 340–351.

36 X. Li, Q. Dong, Q. Tian, A. Sial, H. Wang, H. Wen, B. Pan, K. Zhang, J. Qin and C. Wang, Recent advance in metal- and covalent-organic framework-based photocatalysis for hydrogen evolution, *Mater. Today Chem.*, 2022, **26**, 101037.

37 B. Zhu, R. Zou and Q. Xu, Metal–Organic Framework Based Catalysts for Hydrogen Evolution, *Adv. Energy Mater.*, 2018, **8**, 1801193.

38 S. Navalón, A. Dhakshinamoorthy, M. Álvaro, B. Ferrer and H. García, Metal–Organic Frameworks as Photocatalysts for

Solar-Driven Overall Water Splitting, *Chem. Rev.*, 2023, **123**, 445–490.

39 X. Wang, Y. Peng, S. Yang, H. G. Yang and Y. Hou, Recent progress in metal halide perovskite photocatalysts for hydrogen evolution, *Mater. Chem. Front.*, 2023, **7**, 4635–4657.

40 A. G. Al-Gamal, F. Yehia, M. R. Elmasry, M. A. Abo El-Khair, H. S. Kandeel, A. M. Elseman, D.-H. Kim, K. I. Kabel, S. Kandeel, A. M. Elseman, D.-H. Kim and K. I. Kabel, Perovskite materials for hydrogen evolution: processes, challenges and future perspectives, *Int. J. Hydrogen Energy*, 2024, **79**, 1113–1138.

41 E. Nikoloudakis, I. López-Duarte, G. Charalambidis, K. Ladomenou, M. Ince and A. G. Coutsolelos, Porphyrins and phthalocyanines as biomimetic tools for photocatalytic H_2 production and CO_2 reduction, *Chem. Soc. Rev.*, 2022, **51**, 6965–7045.

42 J. S. O'Neill, L. Kearney, M. P. Brandon and M. T. Pryce, Design components of porphyrin-based photocatalytic hydrogen evolution systems: a review, *Coord. Chem. Rev.*, 2022, **467**, 214599.

43 E. Genc Acar, A. C. Yüzer, G. Kurtay, G. Yanalak, E. Harputlu, E. Aslan, K. Ocakoglu, M. Güllü, M. Ince and I. H. Patir, Improving the photocatalytic hydrogen generation using nonaggregated zinc phthalocyanines, *ACS Appl. Energy Mater.*, 2021, **4**, 10222–10233.

44 S. A. Balogun, D. Thole, D. Masekela and K. D. Modibane, Cobalt phthalocyanine-based photo/electrocatalysts for hydrogen evolution reaction, *Adv. Energy Sustainable Res.*, 2024, **5**, 2400169.

45 H.-Q. Yuan, H.-H. Wang, J. Kandhadi, H. Wang, S.-Z. Zhan and H.-Y. Liu, Electrochemical and photocatalytic hydrogen evolution by an electron-deficient cobalt tris(ethoxycarbonyl)-corrole complex, *Appl. Organomet. Chem.*, 2017, **31**, e3773.

46 W. Auwärter, D. Écija, F. Klappenberger and J. V. Barth, Porphyrins at interfaces, *Nat. Chem.*, 2015, **7**, 105–120.

47 G. B. Bodedla, M. Imran, J. Zhao, X. Zhu and W.-Y. Wong, Design AIEgen-based heterogeneous porphyrin photocatalytic for hydrogen efficient evolution, *Aggregate*, 2023, **4**, e364.

48 K. Zheng, G. B. Bodedla, Y. Hou, J. Zhang, R. Liang, J. Zhao, D. Lee Phillips and X. Zhu, Enhanced cocatalyst-free photocatalytic H_2 evolution by the synergistic AIE and FRET for an Ir-complex conjugated porphyrin, *J. Mater. Chem. A*, 2022, **10**, 4440–4445.

49 D. N. Tritton, G. B. Bodedla, G. Tang, J. Zhao, C.-S. Kwan, K. C.-F. Leung, W.-Y. Wong and X. Zhu, Iridium motif linked porphyrins for efficient light-driven hydrogen evolution via triplet state stabilization of porphyrin, *J. Mater. Chem. A*, 2020, **8**, 3005–3010.

50 G. B. Bodedla, W.-Y. Wong and X. Zhu, Coupling of a new porphyrin photosensitizer and cobaloxime cocatalyst for highly efficient photocatalytic H_2 evolution, *J. Mater. Chem. A*, 2021, **9**, 20645–20652.

51 G. B. Bodedla, J. Huang, W.-Y. Wong and X. Zhu, Self assembled naphthalimide-substituted porphyrin nanowires for photocatalytic hydrogen evolution, *ACS Appl. Nano Mater.*, 2020, **3**, 7040–7046.

52 G. B. Bodedla, L. Li, Y. Che, Y. Jiang, J. Huang, J. Zhao and X. Zhu, Enhancing photocatalytic hydrogen evolution by intramolecular energy transfer in naphthalimide conjugated porphyrins, *Chem. Commun.*, 2018, **54**, 11614–11617.

53 G. B. Bodedla, G. Tang, J. Zhao and X. Zhu, A thiophene bridged naphthalimide–porphyrin complex with enhanced activity and stability in photocatalytic H_2 evolution, *Sustainable Energy Fuels*, 2020, **4**, 2675–2679.

54 V. Piradi, F. Yan, X. Zhu and W.-Y. Wong, A recent overview of porphyrin-based π-extended small molecules as donors and acceptors for high-performance organic solar cells, *Mater. Chem. Front.*, 2021, **5**, 7119–7133.

55 Y. Gao, V. Piradi, X. Zhu and S. K. So, Palladium(II) and platinum(II) porphyrin donors for organic photovoltaics, *ACS Appl. Energy Mater.*, 2022, **5**, 4916–4925.

56 V. Piradi, Y. Gao, F. Yan, M. Imran, J. Zhao, X. Zhu and S. K. So, Thiophene–perylenediimide bridged dimeric porphyrin donors based on the donor–acceptor–donor structure for organic photovoltaics, *ACS Appl. Energy Mater.*, 2022, **5**, 7287–7296.

57 G. B. Bodedla, V. Piradi, M. Imran, J. Zhao, X. Zhu and W.-Y. Wong, Visible-to-near-infrared light-harvesting A–π–D–π–A porphyrins for boosted photocatalytic hydrogen evolution, *J. Mater. Chem. A*, 2023, **11**, 1473–1481.

58 V. Piradi, X. Xu, Z. Wang, J. Ali, Q. Peng, F. Liu and X. Zhu, Panchromatic ternary organic solar cells with porphyrin dimers and absorption-complementary benzodithiophene based small molecules, *ACS Appl. Mater. Interfaces*, 2019, **11**, 6283–6291.

59 V. Piradi, G. Zhang, T. Li, M. Zhang, Q. Peng, X. Zhan and X. Zhu, Side-chain engineering of benzodithiophene-bridged dimeric porphyrin donors for all-small-molecule organic solar cells, *ACS Appl. Mater. Interfaces*, 2020, **12**, 41506–41514.

60 V. Piradi, X. Xu, Q. Peng and X. Zhu, Diketopyrrolopyrrole linked porphyrin dimers for visible-near-infrared photoresponsive nonfullerene organic solar cells, *Mater. Adv.*, 2020, **1**, 2520–2525.

61 V. Piradi, G. Feng, M. Imran, J. Zhao, F. Yan and X. Zhu, Indacenodithiophene bridged dimeric porphyrin donor and absorption complementary indacenodithiophene acceptor for nonfullerene organic photovoltaics, *ACS Appl. Energy Mater.*, 2023, **6**, 3032–3041.

62 V. Piradi, X. Xu, H. Yin, J. K. W. Ho, F. Yan, Q. Peng, S. K. So and X. Zhu, Highly semitransparent indoor nonfullerene organic solar cells based on benzodithiophene-bridged porphyrin dimers, *Energy Technol.*, 2022, **10**, 2100908.

63 A. M. Huerta-Flores, G. Bengasi, K. Baba and N. D. Boscher, Fused porphyrin thin films as heterogeneous visible-light active photocatalysts with well-defined active metal sites for hydrogen generation, *ACS Appl. Energy Mater.*, 2020, **3**, 9848–9855.

64 D. Khusnutdinova, B. L. Wadsworth, M. Flores, A. M. Beiler, E. A. Reyes Cruz, Y. Zenkov and G. F. Moore, Electrocatalytic

properties of binuclear Cu(II) fused porphyrins for hydrogen evolution, *ACS Catal.*, 2018, **8**, 9888–9898.

65 S. Chen, L. Xiao, X. Zhu, X. Peng, W.-K. Wong and W.-Y. Wong, Solution-processed new porphyrin-based small molecules as electron donors for highly efficient organic photovoltaics, *Chem. Commun.*, 2015, **51**, 14439–14442.

66 K. R. J. Thomas and G. B. Bodedla, T-shaped benzimidazole derivatives as blue-emitting materials: the role of C2 substituents on photophysical properties, *Asian J. Org. Chem.*, 2018, **7**, 729–738.

67 G. B. Bodedla, H. Wang, S. Chang, S. Chen, T. Chen, J. Zhao, W.-K. Wong and X. Zhu, β-Functionalized imidazol-fused porphyrin-donor-based dyes: effect of π-linker and acceptor on optoelectronic and photovoltaic properties, *ChemistrySelect*, 2018, **3**, 2558–2564.

68 G. B. Bodedla, K. R. Justin Thomas, M.-S. Fan and K.-C. Ho, The benzimidazole-branched isomeric dyes: effect of molecular constitution on photophysical, electrochemical, and photovoltaic properties, *J. Org. Chem.*, 2016, **81**, 640–653.

69 G. B. Bodedla, V. Piradi, W. Thor, K.-L. Wong, X. Zhu and W.-Y. Wong, Self-assembly of Pt(II) tetrakis(pentafluorophenyl)porphyrin *via* F···F interaction for efficient co-catalyst-free photocatalytic hydrogen evolution, *J. Mater. Chem. A*, 2024, **12**, 2924–2931.

70 G. B. Bodedla, Y. Dong, G. Tang, J. Zhao, F. Zhang, X. Zhu and W.-Y. Wong, Long-lived excited states of platinum(II)-porphyrins for highly efficient photocatalytic hydrogen evolution, *J. Mater. Chem. A*, 2022, **10**, 13402–13409.

71 G. B. Bodedla, M. Imran, J. Zhao, X. Zhu and W.-Y. Wong, Efficient synthesis of porphyrin–iridium complex for enhanced cocatalyst-free photocatalytic hydrogen evolution, *ChemCatChem*, 2025, **17**, e00950.